Journal of the Mechanical Behavior of Biomedical Materials 76 (2017) 153–163

Contents lists available at ScienceDirect

Journal of the Mechanical Behavior of Biomedical Materials

journal homepage: www.elsevier.com/locate/jmbbm

Synergistic structures from magnetic freeze casting with surface magnetized alumina particles and platelets

Michael B. Frank[a,*,1], Sze Hei Siu[b,1], Keyur Karandikar[a], Chin-Hung Liu[a], Steven E. Naleway[c], Michael M. Porter[d], Olivia A. Graeve[a,b], Joanna McKittrick[a,b]

[a] Materials Science and Engineering Program, USA
[b] Department of Mechanical and Aerospace Engineering University of California, San Diego, 9500 Gilman Drive, La Jolla, CA 92093, USA
[c] Department of Mechanical Engineering University of Utah, 1495 E 100 S, Salt Lake City, UT 84112, USA
[d] Department of Mechanical Engineering Clemson University, Clemson, SC 29634, USA

ARTICLE INFO

Keywords:
Freeze casting
Ferrofluid
Magnetic alignment
Platelets
Particles
Ceramic scaffold
Mechanical properties

ABSTRACT

Magnetic freeze casting utilizes the freezing of water, a low magnetic field and surface magnetized materials to make multi-axis strengthened porous scaffolds. A much greater magnetic moment was measured for larger magnetized alumina platelets compared with smaller particles, which indicated that more platelet aggregation occurred within slurries. This led to more lamellar wall alignment along the magnetic field direction during magnetic freeze casting at 75 mT. Slurries with varying ratios of magnetized particles to platelets (0:1, 1:3, 1:1, 3:1, 7:1, 1:0) produced porous scaffolds with different structural features and degrees of lamellar wall alignment. The greatest mechanical enhancement in the magnetic field direction was identified in the synergistic condition with the highest particle to platelet ratio (7:1). Magnetic freeze casting with varying ratios of magnetized anisotropic and isotropic alumina provided insights about how heterogeneous morphologies aggregate within lamellar walls that impact mechanical properties. Fabrication of strengthened scaffolds with multi-axis aligned porosity was achieved without introducing different solid materials, freezing agents or additives. Resemblance of 7:1 particle to platelet scaffold microstructure to wood light-frame house construction is framed in the context of assembly inspiration being derived from both natural and synthetic sources.

1. Introduction

Ordered assembly of isotropic and anisotropic ceramic morphologies into macrostructures with enhanced electrical, piezoelectric and mechanical properties is a significant materials science challenge. Alignment of crystallographic orientation along a preferred axis can be initiated by hot forging (Takenaka and Sakata, 1980; Yoshizawa et al., 2001), strong magnetic field (Inoue et al., 2003; Lee et al., 2015; Ozen et al., 2016; Sakka and Suzuki, 2005; Suzuki et al., 2013; Suzuki and Sakka, 2002a, 2002b; Suzuki et al., 2006; Vriami et al., 2015; Wu et al., 2014; Yang et al., 2015), electrophoretic deposition (Vriami et al., 2015; Zhang et al., 2010) and various forms of casting (tape, gel, slip and centrifugal) (Amorin et al., 2008; Chang et al., 2013; Hall et al., 2001; Kan et al., 2003; Ozer et al., 2006; Paek et al., 2002; Seabaugh et al., 1997; Snel et al., 2009; Suvaci et al., 1999; Takatori et al., 2016; Wei et al., 2005). Carisey et al. (1995a, 1995b) were first to produce monolithic alumina with improved strength and resistance to crack propagation using a tape casting method that controlled the texture of 5–10 wt% alumina platelet seeds within a matrix of alumina particles and organic binders. Shear forces from the straight edge of the sweeping doctor blade oriented the platelets in a preferred alignment before templated grain growth (TGG) occurred during sintering to improve the mechanical properties. When used within polymer composites, alumina platelets can also be aligned to resemble strengthened, bioinspired nacre-like brick-and-mortar microstructures by tape casting (Abba et al., 2016) or low magnetic field (Niebel et al., 2016) following surface magnetization (Erb et al., 2012).

Macroporous ceramics (porosity > 50%) are useful for applications able to withstand a wide range of extreme environments, both thermal and chemical (Studart et al., 2006). Rapid advancements in development of polymer-derived ceramic materials have enabled designs with complex porosity and shapes via manufacturing methods such as soft lithography micromolding (Kamperman et al., 2009), stereolithography and self-propagating photopolymer waveguide technology (Eckel et al., 2016). Potential uses for these structural ceramics with ordered porosity include size selective catalysis and ceramic sandwich panels for

* Corresponding author.
E-mail address: mbfrank@ucsd.edu (M.B. Frank).
[1] M.B. Frank and S.H. Siu contributed equally to this work.

http://dx.doi.org/10.1016/j.jmbbm.2017.06.002
Received 31 March 2017; Received in revised form 31 May 2017; Accepted 1 June 2017
Available online 03 June 2017
1751-6161/

aerospace vehicles. Ceramic water filters (Plappally et al., 2011), made with natural materials (clay, water, sawdust, flour, etc.) using 19th century manufacturing methods, have micron sized pores to capture bacteria associated with water borne diseases (du Preez et al., 2008). Impregnation of the pores with colloidal silver was shown to further deactivate and remove up to 100% of applied bacteria in a controlled study (Oyanedel-Craver and Smith, 2008), although the randomly oriented porosity often makes the filters susceptible to breakage during transportation or use. Nanoporous anodic aluminum oxide (AAO) (Smith, 1974) has similar biofiltration applications (Popat et al., 2004), however, the thin ceramic membranes are not considered robust materials.

Porous ceramic scaffolds strengthened by uniaxial aligned pores can be fabricated by a physical process known as freeze casting (Zhang et al., 2005; Deville et al., 2006; Munch et al., 2008; Naleway et al., 2016). As shown in Fig. 1a, a slurry consisting of a solid phase (e.g., ceramic particles) and freezing agent (e.g., water) uses ice crystal growth to separate particles into lamellae aligned along the freezing direction (z-axis) and oriented randomly along transverse directions (x, y-axes). The frozen block is freeze dried and sintered to strengthen the scaffold structure through densification. A temperature gradient applied to the freezing stage (Bouville et al., 2014a, 2014b; Bai et al., 2015; Bai et al., 2016) along the y-axis can induce long range transverse lamellae alignment that enhances scaffold mechanical properties. Both alumina particles (Tallon et al., 2009; Miller et al., 2015; Tan et al., 2016; Ghosh et al., 2016) and platelets (Hunger et al., 2013; Hunger et al., 2013; Bouville et al., 2014c) have been used for freeze casting without a magnetic field. Freeze casting with particle and platelet mixtures incorporated intralamella and interlamella platelets to stiffen and strengthen scaffolds along the z-axis (Ghosh et al., 2016, 2017). For temperature gradient freeze casting, an alumina particle and platelet mixture, plus a small amount of silica-calcia as liquid phase interface, contributed to TGG (Bouville et al., 2014). Significantly enhanced scaffold mechanical properties were obtained for slurries with a ≈ 9:1 particle to platelet ratio (Bouville et al., 2014; Ghosh et al., 2016), while peak stress values occurred at a higher particle to platelet ratio (19:1) before dissipating when component disparity became too great (39:1) (Ghosh et al., 2017).

A transverse static (along the y-axis) or rotating (about the z-axis) magnetic field applied to slurries of ceramic particles mixed with ferromagnetic magnetite during freeze casting can lead to enhanced lamellae alignment (Porter et al., 2012, 2015, 2016). For a slurry mixture of paramagnetic titania and ferromagnetic magnetite subjected to a static field (≈ 120 mT), interparticle interactions resulted in lamellae alignment and mechanically enhanced scaffolds along the y-axis (Porter et al., 2012). Superparamagnetic magnetite (≈ 10 nm), by itself (Andreu et al., 2011) undergoes chain formation in water only when magnetic interaction energy for a sufficient volume fraction exceeds thermal energy (Faraudo et al., 2013; Faraudo et al., 2016). Similarly, a transverse magnetic field applied during freeze casting to a slurry of surface magnetized alumina can lead to aggregation within aligned lamellae along the y-axis (Fig. 1b). Larger surface magnetized alumina particles (≈ 350 nm) demonstrated more lamellae alignment during magnetic freeze casting than did smaller alumina (≈ 195, 225 nm) and scaffolds had twice the stiffness along the y-axis (≈ 75 mT) compared with no magnetic field (Frank et al., 2017).

This work investigates the use of magnetic freeze casting to construct multi-axis stiffened porous scaffolds with surface magnetized alumina particles and platelets. A wide range of alumina particle to platelet ratios (0:1, 1:3, 1:1, 3:1, 7:1, 1:0) was used to explore how dissimilar morphologies can aggregate in a mechanically synergistic manner during freeze casting with a transverse applied magnetic field along the y-axis. Superparamagnetic magnetite nanoparticles adsorbed onto larger alumina imparts magnetization at the nanoscale, which facilitates control over assembly at the microscale. Examination of spider silk, nacre and bone reveals that the microstructure and hierarchical architecture of these natural materials are responsible for the extraordinary mechanical properties (Aizenberg and Fratzl, 2013; Wegst et al., 2015). Fabrication of bioinspired structural materials by magnetic freeze casting can further correlate with well-established engineering designs observed in light-frame construction of houses made with wood studs and sheathing. Structural materials of the future may yet incorporate a combination of successful design strategies observed among natural wonders as well as the byproducts of manmade civilization that exist all around us.

2. Materials and methods

2.1. Particle and platelet surface magnetization

α-Alumina particles (≈ 350 nm measured by dynamic light scattering technique (DLS) (Frank et al., 2017; Graeve et al., 2010, 2013; Vargas-Consuelos et al., 2014; Cahill et al., 2014; Saterlie et al., 2011, 2012; Fathi et al., 2012); CR6, Baikowski, Malakoff, TX, USA) and platelets (≈ 5 µm diameter, ≈ 200 nm thickness estimated by supplier; YFA5025, Serath, Kinsei Matec Co., Ltd., Osaka, Japan) with bulk density of 3960 kg/m^3 (Ghosh et al., 2016) were surface magnetized following a previously described protocol (Frank et al., 2017). Selected particle and platelet sizes had larger measured magnetic moments relative to smaller particles (≈ 195, 225 nm) and platelets (≈ 600 nm diameter, ≈ 60 nm thickness; ≈ 2 µm diameter, 40 nm thickness) considered in preliminary work not included here. 2.5 g of alumina particles or platelets were stirred in 75 mL distilled water. Dropwise addition of 100 µL anionic ferrofluid (EMG-705, Ferrotec, Bedford, NH, USA), diluted in 5 mL distilled water, to the stirring slurry changed the white alumina particles or platelets to a light brown color. The surrounding solution became clear after stirring for 12 h. Surface magnetized alumina (platelets in Fig. 2, particles in (Frank et al., 2017)) was then rinsed with distilled water, vacuum filtered and dried for 12 h at 100 °C before magnetic freeze casting.

2.2. Magnetic materials characterization

Magnetized alumina particles or platelets (≈ 15–30 mg) were characterized with a vibrating sample magnetometer (VSM, VersaLab, Quantum Design International, San Diego, CA, USA). Mass

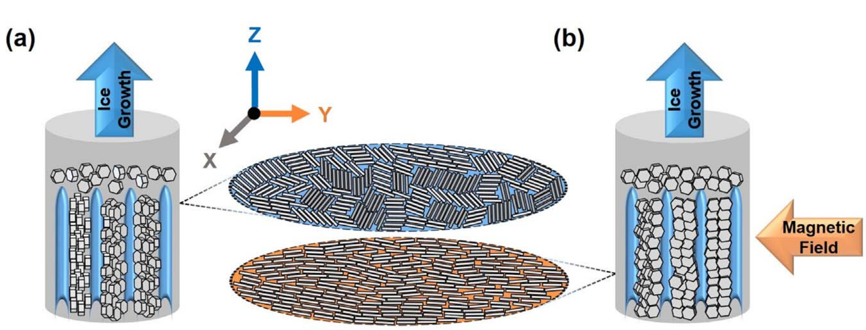

Fig. 1. Schematics for platelets undergoing freeze casting (left, blue oval) and with an applied magnetic field (right, orange oval). (a) Volumetric expansion of ice within a confined mold aligns alumina platelets by shear along the ice growth direction (z-axis). (b) An applied magnetic field aligns magnetized platelets prior to ice solidification along an additional transverse direction (y-axis).

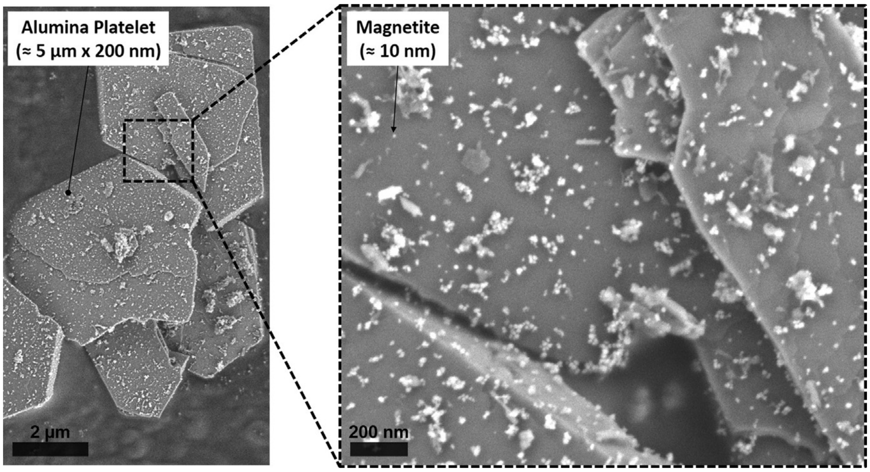

Fig. 2. Scanning electron micrographs of magnetized alumina platelets (≈ 5 µm diameter, ≈ 200 nm thickness) show magnetite nanoparticles (≈ 10 nm) adhered on the surface.

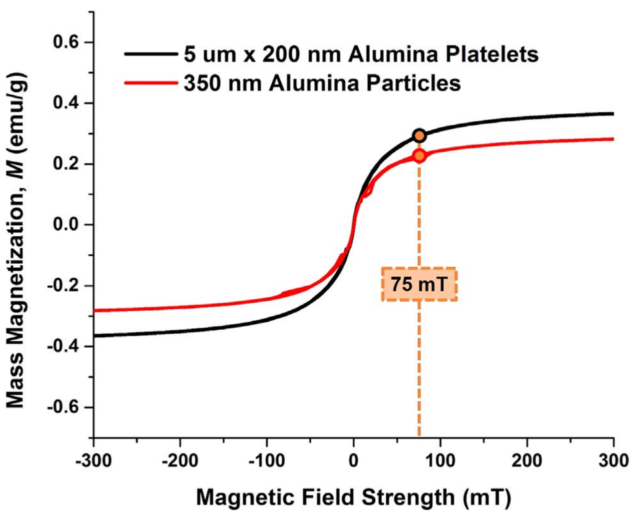

Fig. 3. Comparison of mass magnetization, M, values determined with Eq. (1) using magnetometer measurements for surface magnetized alumina particles (red) and platelets (black) subjected to a sweeping magnetic field, H (units converted to mT). Values for M at the applied magnetic field strength (75 mT) during magnetic freeze casting are indicated.

magnetization (M, emu/g) in response to a sweeping magnetic field (0–3000 Oe, Fig. 3), as well as magnetic moment (m, Am^2) calculated from measured particle volume (v) by DLS (particles) or supplier estimated volume (platelets) were determined with Eqs. (1) and (2).

$$M = \frac{moment}{sampleweight} \tag{1}$$

$$m = v \times M \tag{2}$$

The methodology for calculating the number of magnetite nanoparticles per alumina particle or platelet, as well as the corresponding magnetization value of an individual magnetized particle or platelet, is detailed in Supplementary Fig. 1.

2.3. Magnetized slurry preparation

Slurries of magnetized alumina particles, platelets or combined particles and platelets (10 vol%, particle to platelet ratios of 0:1, 1:3, 1:1, 3:1, 7:1, 1:0) were prepared (by weight alumina) with organic binders, 1 wt% polyvinyl alcohol (100,000 g/mol molecular weight (MW), Alfa Aesar, Ward Hill, MA, USA) and 1 wt% polyethylene glycol (PEG, 10,000 g/mol MW, Alfa Aesar, Ward Hill, MA, USA), and 1 wt% anionic dispersant (Darvan 811, R. T. Vanderbilt Company, Inc., Norwalk, CT, USA). Alumina grinding media was added and the slurry was ball milled for 24 h.

2.4. Magnetic freeze casting

A vise grip (Panavise, Reno, NV) with ≈ 420 mT bar magnets (N52 grade, K & J Magnetics, Inc. Pipersville, PA, USA) attached to either end was placed 7 cm apart along the transverse y-axis using a previously described setup (Frank et al., 2017). Magnetic field strength at the midpoint between the bar magnets surrounding the polyvinyl chloride (PVC) mold containing the slurry was measured with a Gauss meter to be ≈ 75 mT. Freeze casting with a magnetized alumina slurry was conducted either with a magnetic field (≈ 75 mT) along the y-axis or with no magnetic field. A grooved edge filed on the inside wall of the PVC mold was aligned with the bar magnets to provide a visual indicator for the applied magnetic field along the y-axis in sintered samples.

After ball milling, the magnetized alumina slurry was degassed for 15 min by vacuum before 5 mL was poured into a PVC mold and centered underneath the magnetic field apparatus. Freezing occurred from the bottom upward using a previously described freeze casting device (Porter et al., 2012) and freezing front velocity (FFV) was estimated as the total frozen scaffold height (≈ 45 mm) divided by the total freezing time (≈ 1800 s) to get FFV ≈ 25 µm/s (Ghosh et al., 2016, 2017). Frozen samples were lyophilized with a bench-top freeze dryer (Labconco, Kansas City, MO, USA) at -50 °C and 3.5×10^{-6} Pa for 48 h to sublime ice crystals and leave behind fragile 'green body' scaffolds made up of alumina particles, platelets or both that were held together by polymer binders. Samples were sintered in an open air furnace for 3 h at 1500 °C with heating and cooling rates of 2 °C/min following a previously reported procedure (Porter et al., 2012).

2.5. Mechanical characterization

Six scaffolds were prepared for each condition with alumina particle to platelet ratio (0:1, 1:3, 1:1, 3:1, 7:1, 1:0) and magnetic field strength (0, 75 mT) as variables. Compression testing of the scaffolds was performed on a 3342 Instron materials testing machine (Instron, Norwood, MA) with a 500 N static load cell at a constant crosshead velocity of 0.005 mm/s following previous procedures (Porter et al., 2012, 2016; Frank et al., 2017; Porter et al., 2014; Naleway et al., 2015). Three samples (≈ 5 mm^3 cubes) cut from each scaffold center, where uniform porosity was evident, were compressed in the transverse (x-axis), magnetic field (y-axis) and ice growth (z-axis) directions for each particle to platelet ratio condition (1:3, 1:1, 3:1, 7:1), while two samples were compressed in the y-axis and z-axis for the all particles (1:0) and all platelets (0:1) conditions. Ultimate compressive strength and Young's modulus were determined from the maximum stress and linear slope of the stress–strain curves, respectively.

2.6. Scanning electron microscopy characterization

Two of the six sintered scaffolds for each condition were sectioned at midpoint height, mounted to a stage and coated with colloidal graphite along the bottom and side walls. Iridium was sputter coated (EMITech K575X, Quorum Technologies Ltd., West Sussex, UK) for 15 s at 85 mA onto the top. Scanning electron microscopy (SEM) micrographs at 10 kV (spot size 3 nm) from a Philips XL30 field emission environmental scanning electron microscope (FEI-XL30, FEI Company, Hillsboro, OR) were stitched together along overlapping edges to assess long range lamellar wall alignment in the scaffold center. Lamellar wall regions were shaded different colors to indicate horizontal alignment (light blue, 22.5° offset from the *y*-axis), angled alignment (yellow, 22.5° to 67.5° offset from the *y*-axis) and no alignment (red, 67.5° to 90° offset from the *y*-axis). ImageJ software (National Institutes of Health, Bethesda, MD, USA) was used to quantify lamellar wall horizontal alignment, for the overlapped SEM micrographs area (6000 µm x 2700 µm) at 100x magnification within the scaffold center region used for mechanical testing, by dividing the light blue shaded scaffold area by the total scaffold area.

Scaffold morphology was further characterized using ImageJ to analyze 500x magnification micrographs from the center region of each condition. The number of bridges between lamellar walls per unit area (bridge density, ρ_b) and the average wavelength (λ) from measurements ($N = 40$) of adjacent lamellae top surfaces were input into Eq. (3) to obtain a dimensionless parameter (m_s) for describing scaffold morphology as either lamellar ($m_s > 5$), dendritic ($1 < m_s < 5$) or isotropic ($m_s < 1$) (Naglieri et al., 2013), as shown in Supplementary Fig. 2.

$$m_s = \frac{(1/\rho_b)}{\lambda^2} \tag{3}$$

3. Results and discussion

3.1. Magnetic response of magnetized alumina particles and platelets

Magnetized alumina particles and platelets subjected to a sweeping magnetic field, *H*, and plotted versus *M* (Eq. (1), Fig. 3) had an absence of hysteresis and magnetization at $H = 0$ on the *M-H* curve. This result confirmed the magnetized particles and platelets “responded” to a sweeping magnetic field in a superparamagnetic manner (see Supplementary Materials from (Frank et al., 2017)) with less susceptibility (maximum slope) and saturation (maximum *M* value) than superparamagnetic magnetite nanoparticles alone (Nocera et al., 2012), but with similar magnetic properties as composites with superparamagnetic magnetite cores (Chen et al., 2009). DLS measurement after ball milling indicated ≈ 350 nm average alumina particle size (Frank et al., 2017), while supplier estimates for alumina platelets (≈ 5 µm diameter, ≈ 200 nm thickness) were used due to size complexity for measurement of non-spherical platelet shapes (Bowen et al., 2002; Hayakawa et al., 1998). At 75 mT, calculated magnetic moment, *m*, (Eq. (2)) for platelets was more than 200x greater than for particles due in large part to the platelets having ≈ 175x greater volume.

Since α-alumina particles and platelets with equal weight (2.5 g) and density (3.96 g/cm^3) were magnetized with an equal volume of ferrofluid (0.1 mL), the amount of surface adsorbed magnetite per alumina particle or platelet was estimated based on assumptions for spherical magnetite nanoparticle size (≈ 10 nm) and fraction in ferrofluid (4 vol%), as detailed in Supplementary Fig. 1. Overall, each alumina particle and platelet had ≈ 270 and ≈ 47,500 adsorbed magnetite nanoparticles, respectively. Values of *M* at 75 mT multiplied by the mass of an individual particle or platelet with adsorbed magnetite yielded 1.97×10^{-14} and 4.54×10^{-12} emu magnetization values for surface magnetized particles and platelets, respectively. Magnetization per platelet was ≈ 230x greater than per particle due to the larger platelet size and aspect ratio (≈ 25). Although Faraudo et al. (2016) described chain assembly for only spherical superparamagnetic magnetite nanoparticles or composite particles with superparamagnetic cores, aggregation of magnetized particles and platelets in water should also occur at a sufficient magnetic field strength and volume fraction when the magnetic interaction energy exceeds the thermal energy. Larger platelets have a much greater magnetic moment than smaller particles based on calculations from VSM data, so magnetic freeze casting with platelets should lead to more aggregation for enhanced lamellar wall alignment.

3.2. Lamellar wall alignment

1D chain formation of magnetite nanoclusters subjected to an applied magnetic field at room temperature in aqueous solution has been described (Wang et al., 2009). During magnetic freeze casting, magnetized alumina particles (≈ 350 nm) aggregated into ≈ 20% aligned lamellar walls along the *y*-axis at 75 mT for 3–4 min before ice nucleation occurred within the slurry (Frank et al., 2017). Magnetic freeze cast scaffolds made up of only larger magnetized alumina platelets, which have more than 200x greater magnetic moment per platelet than per particle, displayed more lamellar wall alignment than particle only scaffolds (Frank et al., 2017) along the *y*-axis (Fig. 4). As expected, magnetized alumina platelets at 0 mT displayed no lamellar wall alignment, whereas alignment was evident along the *y*-axis in the scaffold center at 75 mT (Fig. 4a). Examination of a wider view (≈ 2500 µm x ≈ 2000 µm), with colorized regions to indicate lamellar wall orientation, confirmed ≈ 98% alignment of magnetized platelets along the *y*-axis at 75 mT (Fig. 4b).

Ghosh et al. (2016, 2017) did similar freeze casting experiments with slurry mixtures of alumina particles and platelets at FFV ≈ 25 µm/s, but they did not surface magnetize the ceramics nor use a magnetic field to generate lamellar wall alignment of the components along the *y*-axis. They determined that 9:1 and 19:1 alumina particle (≈ 900 nm) to platelet (≈ 8 µm diameter, ≈ 400 nm thickness) slurry ratios were best for orienting intralamella and interlamella platelets in a mechanically advantageous manner along the *z*-axis in freeze cast scaffolds. Scaffolds made primarily of alumina platelets had significantly lower strength in the *z*-axis since slurries with more platelets in direct contact to each other had considerably less particle packing fraction and densification than ones with larger alumina particle to platelet ratios (Ghosh et al., 2017). Uniaxial compression testing was conducted only in the *z*-axis, with no mention of testing or expectation of mechanical strengthening in the *y*-axis. Freeze casting with non-magnetized alumina particle and platelet slurries and no applied magnetic field most likely produced randomly oriented lamellar walls in the *y*-axis.

Since applied magnetic field strength (75 mT) induced aligned aggregation along the *y*-axis for magnetized alumina particles (Frank et al., 2017) and platelets (Fig. 4), slurries with varying particle to platelet ratios (1:3, 1:1, 3:1, 7:1) were freeze cast at FFV ≈ 25 µm/s and compared. SEM micrographs for each platelet and particle condition showed how magnetized particles and platelets were arranged within lamellae of the sintered porous scaffolds at 0 and 75 mT (Fig. 5). Interestingly at 75 mT, only the equivalent particle to platelet ratio (1:1) condition produced no lamellar wall alignment, whereas imbalanced particle to platelet ratios (1:3, 3:1, 7:1) each displayed long range lamellar wall alignment in the *y*-axis. This result indicates that a particle or platelet majority within the slurry must have guided aggregation into chains that formed aligned lamellar walls. The 7:1 particle to platelet condition had the most uniform arrangement of mineral bridges that connected adjacent lamellae. Platelets with much larger size, aspect ratio and magnetic moment than smaller particles are hypothesized to align with the magnetic field and serve as a template for surrounding particle aggregation before ice nucleation occurred. More intralamellar platelets were observed along the *y*-axis within lamellar walls than interlamellar platelets oriented in the *x*-axis within mineral bridges (Fig. 5).

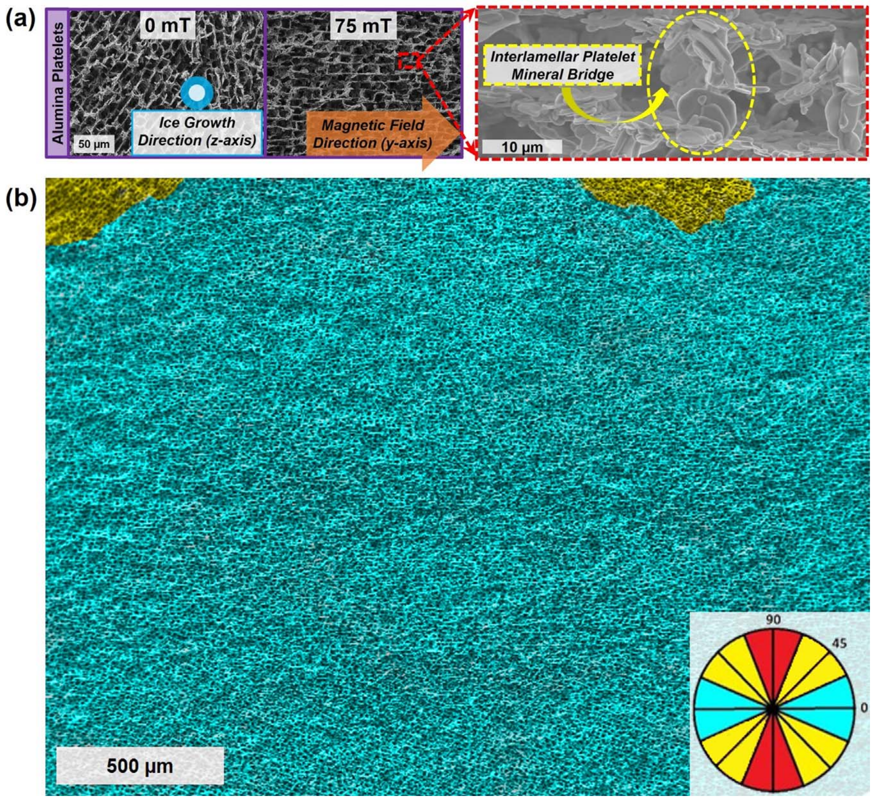

Fig. 4. Scanning electron micrographs from scaffold center regions with and without an applied magnetic field. (a) Lamellar walls for magnetized alumina platelets (≈ 5 µm diameter, ≈ 200 nm thickness) orient randomly at 0 mT, whereas macroscopic alignment in the *y*-axis occurs within the scaffold center at 75 mT. An interlamellar platelet mineral bridge (yellow dashed circle) indicates a non-orthogonal interface with the lamellar walls. (b) Lamellar wall orientation from the scaffold center at 50x magnification (≈ 2500 µm x ≈ 2000 µm) had ≈ 98% alignment (light blue) in the *y*-axis.

Image analysis of stitched together SEM micrographs (6000 µm x 2700 µm) from the center of a 7:1 particle to platelet scaffold indicated ≈ 60% lamellar wall alignment at 75 mT in the *y*-axis (Fig. 6). Comparison with lamellar wall alignment in homogeneous slurries of magnetized particles (≈ 20%) (Frank et al., 2017) and platelets (≈ 98%) in Fig. 4 indicated that a minority of platelets with much larger size and magnetic moment than a majority of particles must have helped magnetic interaction energy sufficiently exceed thermal energy to increase aggregation within *y*-axis aligned lamellar walls. Faraudo et al. (Andreu et al., 2011; Faraudo et al., 2013, 2016) used Langevin Dynamic (LD) simulations to predict kinetics for average superparamagnetic colloid chain length as a function of time. As predicted by LD simulations, exposure of a magnetized slurry to a magnetic field beyond the currently implemented time of 3–4 min prior to ice nucleation should lead to increased chain formation with more lamellar wall alignment in the *y*-axis. Alternative freeze casting methods that use a temperature gradient (Bouville et al., 2014a, 2014b; Bai et al., 2015, 2016) can generate lamellar wall alignment in only one transverse axis, whereas an applied magnetic field can aggregate magnetized materials along multiple axes applied during freezing for fabrication of more complex porous scaffolds.

3.3. Mechanical properties

Mechanical properties of freeze cast alumina particle and platelet scaffolds were dependent on slurry parameters and processing conditions, which differed from Ghosh et al. (2016, 2017) (Table 2). These differences contributed to a lower range of ρ_r values for this work with lower Young's modulus (*E*, MPa) and ultimate compressive strength (UCS, MPa) values in the *z*-axis (Table 1). However, the main objective for this work was to mechanically stiffen scaffolds in the *y*-axis by magnetic freeze casting with magnetized alumina particles and platelets aggregated within aligned lamellar walls. Previous magnetic freeze casting work demonstrated that aligned lamellar walls made up of ≈ 350 nm magnetized alumina particles led to mechanically stiffened scaffolds in the *y*-axis at 75 mT (Frank et al., 2017). Magnetic freeze casting with varying ratio slurries of magnetized alumina particles and platelets at 75 mT enabled further comparison of mechanical property differences in *x*, *y*, and *z*-axes (Fig. 7a).

Although all conditions were prepared with the same freeze casting parameters, slurries with a higher particle to platelet ratio (1:0, 7:1) generally had larger ρ_r values than ones with a lower particle to platelet ratio (0:1, 1:3, 1:1, 3:1) as shown in Table 1. Larger ρ_r resulted in slightly larger *E* and UCS for *x*, *y* and *z*-axes, thus specific modulus, E_r (E / ρ_r), and specific strength, UCS_r (UCS / ρ_r), values were used to account for variability between particle to platelet ratio conditions (Fig. 7). The range of m_s values determined for each particle to platelet ratio condition ($1.4 < m_s < 2.2$) indicated dendritic ($1 < m_s < 5$), not lamellar ($m_s > 1$) or isotropic ($m_s < 1$) structures formed (Supplementary Fig. 2). There were no mechanical property trends evident for compression in the *x*-axis (Fig. 7b). An applied magnetic field (75 mT) noticeably contributed to E_r enhancement in the *y*-axis (Fig. 7c). Interestingly, conditions with more particles than platelets (1:0, 7:1, 3:1) had higher ρ_b values, which most likely contributed to E_r enhancement in the *z*-axis (Fig. 7d). Further examination of each particle to platelet ratio condition revealed that an applied magnetic field did not affect E_r in the *z*-axis. However, E_r in the *z*-axis was enhanced slightly for whichever sample set (0 or 75 mT) had higher ρ_b values (Supplementary Fig. 2) (Table 2).

Representative stress-strain curves for 7:1 particle to platelet conditions in the *y*-axis at 0 and 75 mT are indicated in Fig. 8a. E_r was enhanced by ≈ 125% at 75 mT compared with 0 mT (Fig. 8b), while UCS_r in comparison was enhanced by ≈ 35% (Fig. 8c). This result indicated magnetic field induced aggregation of particles and platelets led to synergistic mechanical stiffening up until brittle failure occurred. These 80–90% porous ceramic scaffolds must have had some lamellar walls and bridges that broke within the "elastic" regime measured as E_r up until overall failure measured as UCS_r occurred in the interconnected porous samples. Measured values for E_r in porous scaffolds,

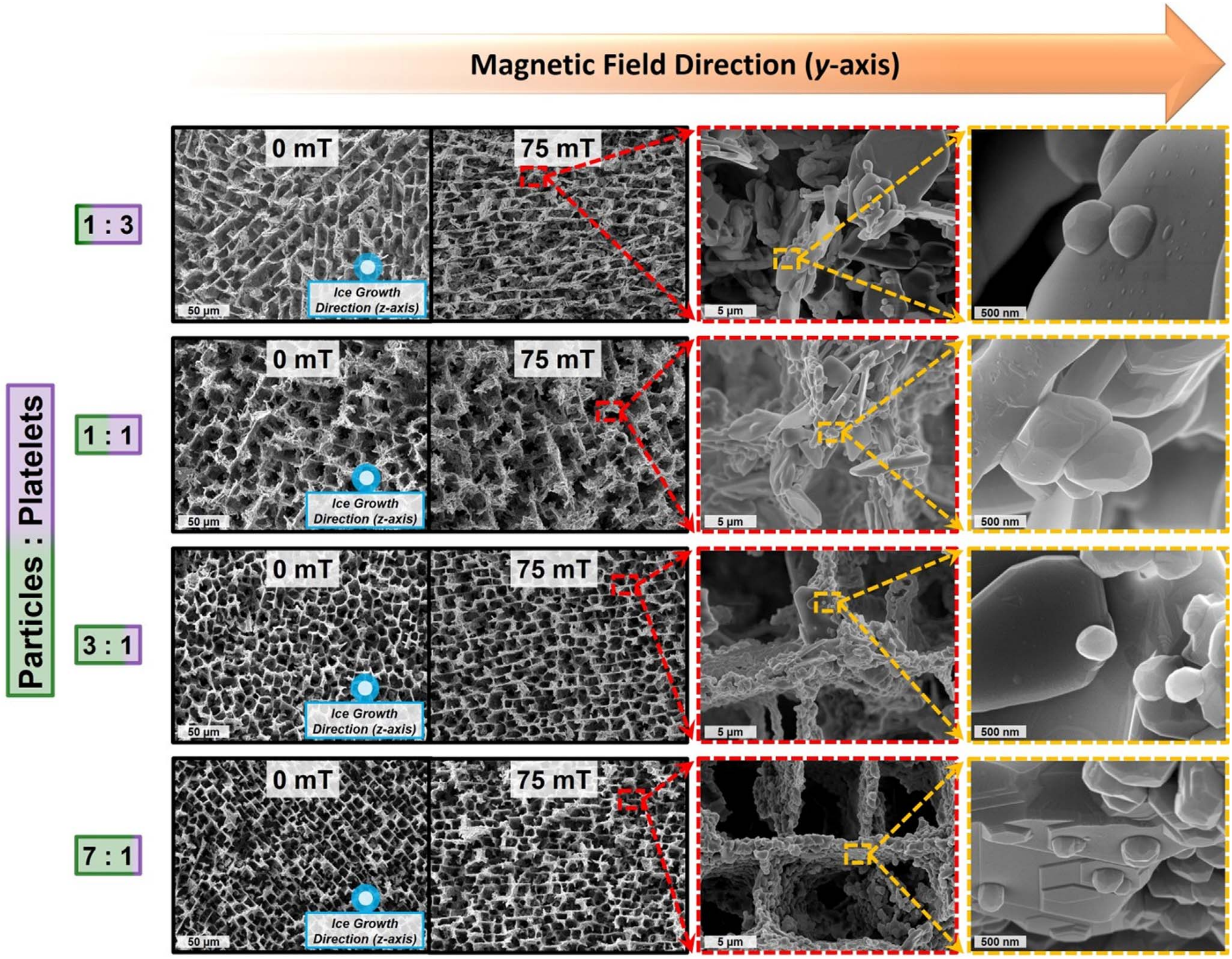

Fig. 5. Scanning electron micrographs of scaffold center regions made from varying ratios of magnetized alumina particles (green) and platelets (purple) freeze cast at 0 or 75 mT. A heterogeneous mixture results in aligned lamellar walls when an imbalance of particles to platelets exists. Lamellar walls were disordered for an equivalent (by weight) particle and platelet slurry at 75 mT, while the most uniform alignment occurred at the same magnetic field strength with a 7:1 particle to platelet ratio.

more so than UCS_r values, were more consistent and thus a better indicator of mechanical enhancement from lamellar wall alignment due to the magnetic field in the *y*-axis. Particle majority scaffolds (0%, 12.5% and 25% platelets) generally had better mechanical properties than platelet majority ones (75, 100% platelets) in the *y*-axis (Fig. 8b, c) due to a greater proportion of interface contact between spherical, rather than high aspect ratio planar, surfaces. For the 7:1 particle to platelet condition, a small number of platelet “seeds” (12.5% platelets),

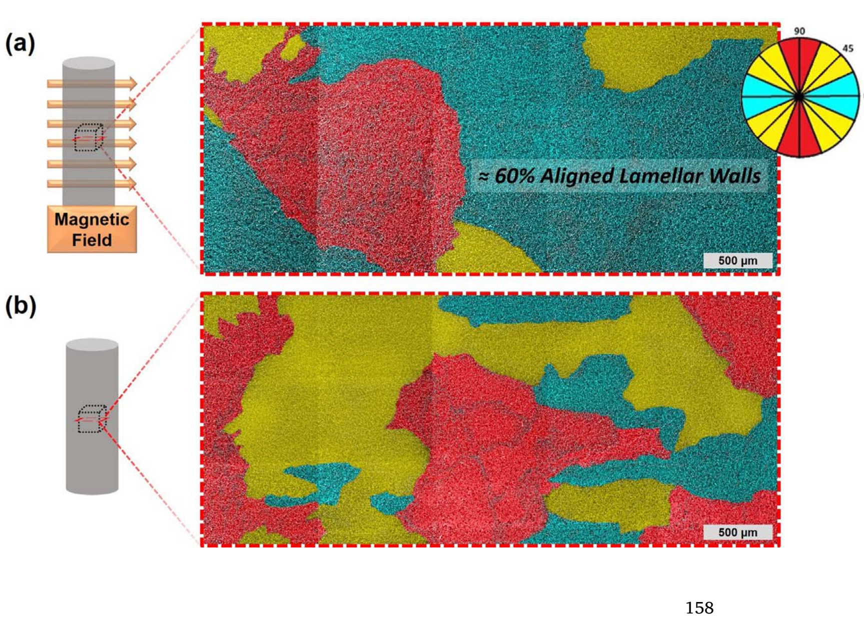

Fig. 6. Long range lamellar wall alignment in the transverse direction (*y*-axis) was evident for freeze cast scaffolds at 75 mT, but not at 0 mT. (a) A 6000 µm x 2700 µm scanning electron micrograph from the scaffold center at 100x magnification was stitched together from a 7:1 particle to platelet scaffold freeze cast at 75 mT. Analysis of lamellar wall orientation with ImageJ software indicated ≈ 60% alignment (light blue). (b) Long range lamellar wall alignment was not evident in the scaffold center for a 7:1 particle to platelet scaffold freeze cast at 0 mT.

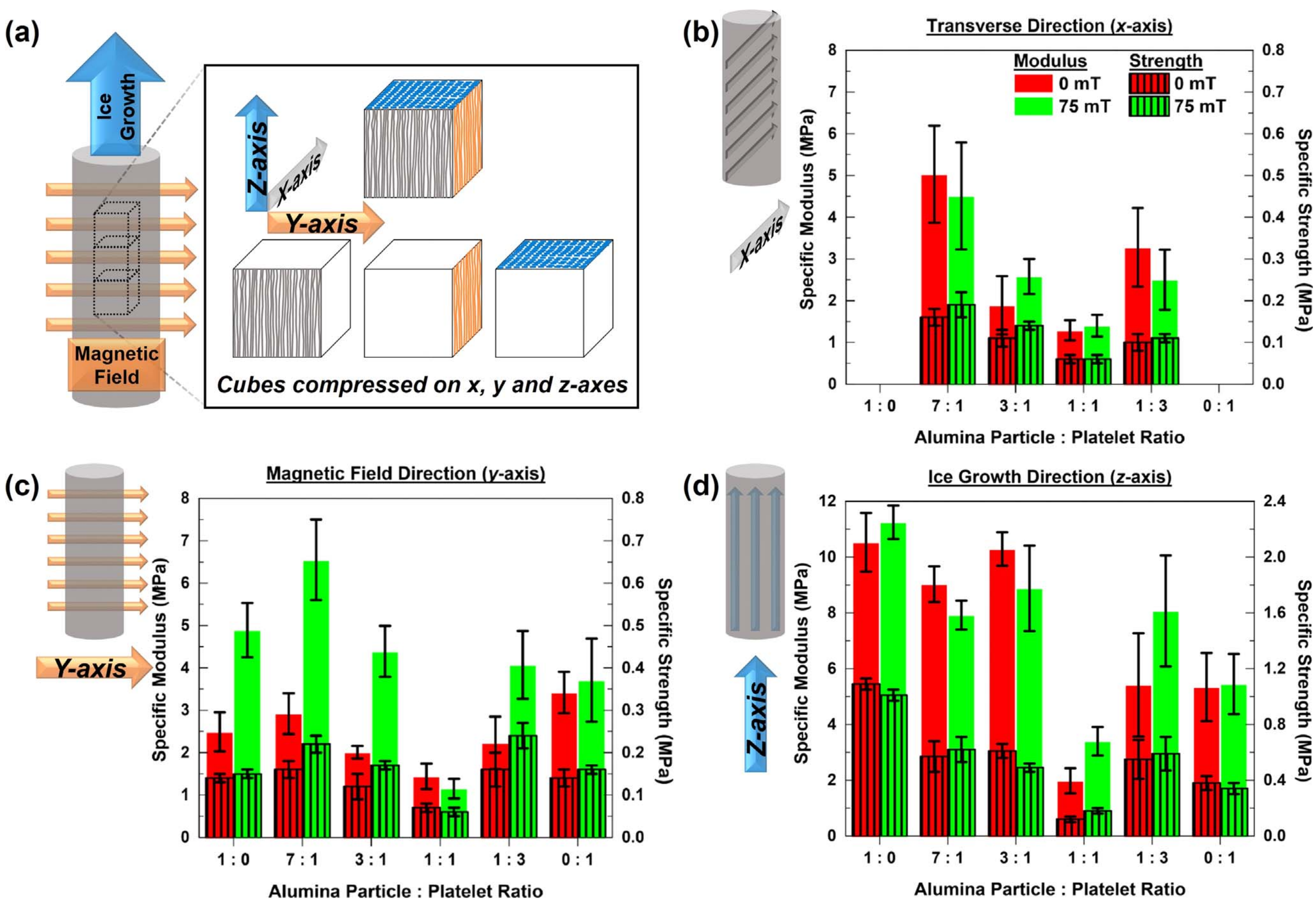

Fig. 7. Comparison of relative density normalized compressive mechanical properties for scaffolds freeze cast at 0 or 75 mT with varying ratios of magnetized alumina particles and platelets (1:0, 7:1, 3:1, 1:1, 1:3, 0:1). (a) Individual cubes from the scaffold center are compressed in the transverse (*x*-axis, gray cube face), magnetic field (*y*-axis, orange cube face) and ice growth (*z*-axis, blue cube face) directions. Specific Young's Modulus (E_r) and ultimate compressive strength (UCS_r) values are obtained from dividing measured values (Table 1) by average relative density (ρ_r) for each condition in the (b) transverse (*x*-axis), (c) magnetic field (*y*-axis) (c) and ice growth (*z*-axis) directions. Data points are the mean of N = 6 measurements with error bars representing ± standard error (standard deviation / √N).

with a much higher magnetic moment, may have aligned first along the magnetic field direction before the majority remainder of particles aggregated around the platelets to demonstrate a type of TGG effect. The best E_r results in the *y*-axis were found for 7:1 particle to platelet ratio scaffolds, so any higher proportion of platelet "seeds" with more lamellar wall alignment was likely offset by less interface contact between the high aspect ratio planar platelets.

For all other conditions, except the 1:1 particle to platelet ratio, E_r

Table 1
Relative density (ρ_r), Young's modulus (E) and ultimate compressive strength (UCS) for alumina scaffolds made with different platelet to particle ratios and freeze cast with or without a static magnetic field (0, 75 mT). Sintered density (ρ^*) was determined from measured mass, measured volume dimensions (≈ 5 mm^3 cubes) and α-alumina bulk density (ρ_s = 3.96 g/cm^3) (Ghosh et al., 2016). Compression occurred along the transverse (*x*-axis), magnetic field (*y*-axis) and ice growth (*z*-axis) directions. Sample size for each condition: N = 6. All data reported are mean ± standard error (standard deviation / √N).

	Mag Field (mT)	Particles: Platelets Ratio (by weight)					
		1:0	7:1	3:1	1:1	1:3	0:1
Relative Density (%)	0	17.5 ± 0.2	15.4 ± 0.1	11.4 ± 0.4	12.4 ± 0.2	13.0 ± 0.6	12.2 ± 0.4
$\rho_r = \rho^*/\rho_s$	75	17.9 ± 0.2	15.3 ± 0.4	12.8 ± 0.4	12.9 ± 0.2	14.3 ± 0.6	12.6 ± 0.1
***E*, MPa, *x*-axis**	0	N/A	77.4 ± 17.8	21.6 ± 8.0	16.0 ± 3.0	42.6 ± 12.2	N/A
	75	N/A	69.0 ± 19.6	33.0 ± 5.4	18.0 ± 3.3	35.8 ± 10.3	N/A
***E*, MPa, *y*-axis**	0	43.6 ± 8.0	45.0 ± 7.4	22.9 ± 1.7	17.9 ± 3.7	29.0 ± 8.0	41.7 ± 6.0
	75	87.5 ± 11.4	100.2 ± 14.6	56.2 ± 7.7	14.8 ± 2.9	58.2 ± 11.4	46.7 ± 12.3
***E*, MPa, *z*-axis**	0	184.2 ± 18.4	139.0 ± 9.9	117.3 ± 6.8	24.5 ± 5.5	70.5 ± 24.0	65.1 ± 14.8
	75	201.4 ± 10.8	121.2 ± 8.0	113.7 ± 19.5	43.9 ± 6.5	115.4 ± 28.4	68.7 ± 13.6
UCS, MPa, *x*-axis	0	N/A	2.52 ± 0.37	1.26 ± 0.28	0.74 ± 0.13	1.28 ± 0.31	N/A
	75	N/A	2.85 ± 0.43	1.82 ± 0.14	0.72 ± 0.13	1.62 ± 0.16	N/A
UCS, MPa, *y*-axis	0	2.43 ± 0.20	2.43 ± 0.30	1.38 ± 0.32	0.81 ± 0.12	2.06 ± 0.54	1.72 ± 0.23
	75	2.75 ± 0.15	3.34 ± 0.32	2.24 ± 0.08	0.81 ± 0.11	3.39 ± 0.41	1.96 ± 0.07
UCS, MPa, *z*-axis	0	19.16 ± 0.57	8.82 ± 1.60	6.95 ± 0.51	1.49 ± 0.20	7.18 ± 1.81	4.69 ± 0.55
	75	18.04 ± 0.70	9.51 ± 1.28	6.31 ± 0.29	2.32 ± 0.22	8.39 ± 1.72	4.34 ± 0.39

Table 2
Particle and platelet slurry parameters and freeze casting processing conditions for Ghosh et al. (2016, 2017) versus this work.

	Ghosh et al. (2016, 2017)	Frank et al. (this work)
Scaffold Length (cm)	≈ 4.5	≈ 4.5
Freezing Front Velocity (FFV, μm/s)	≈ 25	≈ 25
Particle Size (nm)	≈ 900	≈ 350
Platelet Size [Diameter (μm) x Thickness (nm)]	≈ 8 × 400	≈ 5 × 200
Solid Loading (vol%)	15	10
Organic Binder (wt% of solids)	5	2
Dispersant (wt% of solids)	0.5	1
Sintering Temperature (°C)	1550	1500
Sintering Time (Hours)	4	3
Relative Density Range (%)	17–22	11–18

was also enhanced in the y-axis at 75 mT versus 0 mT (Fig. 8b). The 1:1 particle to platelet ratio scaffolds had disordered lamellar walls at 75 mT in the *y*-axis (Fig. 5) and the expectation for no mechanical property improvement was confirmed. However, the 0:1 particle to platelet condition made up of highly ordered platelets within aligned lamellar walls at 75 mT in the *y*-axis (Fig. 4) had only ≈ 10% enhancement of E_r compared with 0 mT (Fig. 8b). Magnetized platelet aggregation at 75 mT accounted for extensive intralamellar platelet ordering along the *y*-axis, but interlamellar platelets within mineral bridges connected between parallel lamellae were not as well ordered along the *x*-axis (Fig. 4b). Non-orthogonal interfaces between intralamellar and interlamellar platelets, as well as lower packing fraction and densification for platelet predominant slurries (Ghosh et al., 2017), led to minimal enhancement of E_r values despite long range lamellar wall alignment evident in the *y*-axis (Fig. 8b).

Fig. 7d shows how E_r and UCS_r values in the *z*-axis exceeded those in the *y*-axis (Fig. 7c) due to ice templated formation of lamellar walls aligned along the ice growth direction. Compression along the *z*-axis can generally cause crack formation and growth due to local lamellar wall buckling (Porter et al., 2014; Munch et al., 2009). Previous work (Frank et al., 2017) showed how magnetic freeze casting with ≈ 350 nm alumina particles and a greater magnetic field strength (150 mT) produced broad aligned lamellar wall regions, similar to larger "grains," which facilitated a greater amount of compressive load distribution more evenly along the *z*-axis compared with smaller "grains" formed at a weaker magnetic field strength (75 mT). However, the orientation of those "grains" was angled more from the *y*-axis along magnetic field lines which emanated from the closer positioned bar magnet poles at 150 mT versus 75 mT. Less mechanical stiffening occurred in the *y*-axis at 150 mT compared with 75 mT because less "grains" made up of aligned lamellar walls were oriented along the *y*-axis (Frank et al., 2017). For this work, E_r and UCS_r at 75 mT were not significantly enhanced compared with 0 mT in the *z*-axis (Fig. 8b, c), but the desired objective for more lamellar wall alignment along the *y*-axis in the scaffold center at 75 mT was met and this resulted in significantly enhanced E_r in the *y*-axis (Fig. 8b).

Comparison with particle and platelet freeze casting results from Ghosh et al. (2016, 2017) began with consideration for the different slurry parameters and freeze casting conditions (Table 2). Among many differences, their use of larger particles (900 nm vs. 350 nm), larger platelets (8 μm × 400 nm vs. 5 μm × 200 nm) and a higher solid loading amount (15 vol% vs. 10 vol%) resulted in SEM micrographs of scaffold cross-sections with much less mineral bridging between lamellar walls. At a comparable freeze front velocity (FFV ≈ 25 μm/s), Ghosh et al. (2017) had $3 < m < 6$ values for particle and platelet mixture conditions which were consistent with their observed lamellar and slightly dendritic structures. At a similar FFV ≈ 25 μm/s, the $1.4 < m < 2.2$ values from this work were consistent with much more dendritic morphology (Supplementary Figure 2). Overall, assessment for how increased platelet percentage affected mechanical properties in the *z*-axis must take into account the big disparities evident in *m* values between this work and Ghosh et al. (2017), which were the result of differences in freeze casting parameters as well as sintering conditions (1550 °C for 4 h vs. 1500 °C for 3 h).

Multi-axis aligned porosity in 7:1 particle to platelet ratio scaffolds occurred due to microstructural arrangement of alumina particle and platelet morphologies by ice crystal growth and an applied magnetic field. A natural macrostructural analog with multi-axis aligned porosity is trabecular bone found in long bones close to joints and within vertebrae (Willie et al., 2013), although the porosity dimensions are an order of magnitude greater than for these scaffolds (hundreds versus tens of microns). At the microstructural level, trabecular bone is a composite that consists of nanoscale carbonated calcium phosphate platelets (dahllite, average length and width 50 × 25 nm) organized within a mineralized collagen matrix into a hierarchical structure with high strength and toughness (Wegst et al., 2015; Weiner and Wagner, 1998). Anatomist Georg Hermann von Meyer and engineer Karl

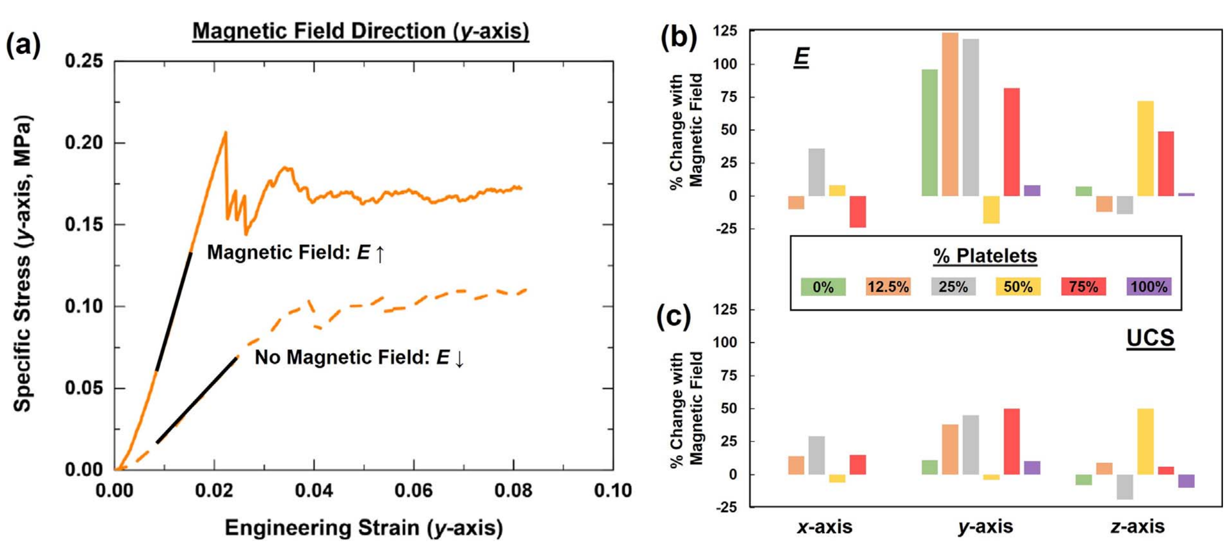

Fig. 8. Applied magnetic field (75 mT) versus no magnetic field (0 mT) expressed as percent change in relative density normalized compressive mechanical properties for particle and platelet mixtures. (a) Representative specific stress-strain curves for 7:1 magnetized alumina particle to platelet (12.5% platelets) scaffolds freeze cast at 75 mT (solid orange line) and 0 mT (dashed orange line) indicate mechanical enhancement due to synergistic aggregation of particles and platelets. Percent change values at 75 mT versus 0 mT for (b) specific Young's Modulus (E_r) and (c) ultimate compressive strength (UCS_r) are shown in the transverse (*x*-axis), magnetic field (*y*-axis) and ice growth (*z*-axis) directions.

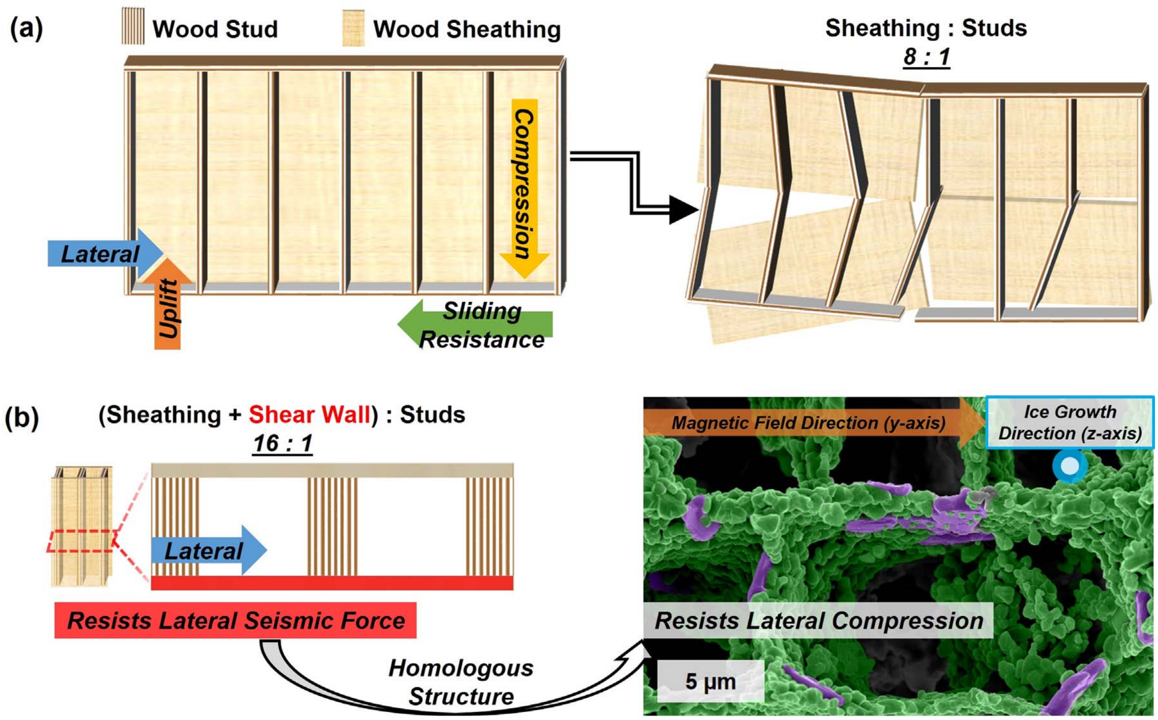

Fig. 9. Schematic of an exterior wall from a light-frame construction house made with wood sheathing and studs compared with a scaffold portion made of alumina particles and platelets. (a) A residential exterior wall has plywood sheathing fastened to wood studs spaced equidistant center-to-center distance apart from each other for an 8:1 width ratio of sheathing to studs. A house can slide, rack or overturn off its foundation due to seismic forces that cause exterior wall failure. (b) An exterior wall retrofit with a shear wall has a 16:1 width ratio of sheathing to studs that provides enhanced lateral seismic force resistance. Intralamellar and interlamellar magnetized alumina platelets (purple) and particles (green) aggregate synergistically during freeze casting at 75 mT. A 7:1 ratio of particles to platelets produced enhanced stiffness in the magnetic field direction. Magnetic freeze cast porous scaffolds are homologous to shear wall reinforced exterior walls in light-frame wood houses by structure (studs and sheathing = mineral bridges and lamellar walls, respectively) and resistance to lateral force.

Culmann proposed a "trajectorial hypothesis", further refined by Julius Wolff and Wilhelm Roux, that trabecular bone porosity follows the trajectories of principal stresses and that bone has the ability to adapt to mechanical stimulus through a "quantitative self-regulating mechanism" (Huiskes, 2000).

Inorganic magnetic freeze cast structures cannot mimic the adaptive multi-functionality of organic trabecular bone, but 7:1 particle to platelet ratio scaffolds at the microstructural level do bear a resemblance to light-frame wood construction that accounts for ≈ 99% of housing in California (Li and Ellingwood, 2007). Conventional walls made with wood studs and drywall cannot withstand multi-axial stresses associated with simultaneous lateral and uplift forces from earthquakes. Shear walls, typically consisting of plywood or gypsum sheathing fastened on either side of wood studs in exterior walls, are the primary lateral seismic force-resisting components in light-frame wood residential construction (Li and Ellingwood, 2007; Li et al., 2010; van de Lindt, 2005; Chen et al., 2010). Homologous lamellar wall (sheathing) and mineral bridge (studs) microstructures evident in 7:1 particle to platelet ratio scaffolds can be compared with an 8:1 (Fig. 9a) or 16:1 (Fig. 9b) width ratio of sheathing to studs in standard or shear wall reinforced residential exterior walls, respectively. Heterogeneous particle and platelet morphologies, made of homogeneous alumina and arranged in a mechanically synergistic manner along the *y*-axis by magnetic freeze casting, can be sintered to make continuous, nearly orthogonal, interfaces between lamellar walls and mineral bridges. Freeze casting that incorporates bioinspiration from ice and trabecular bone can also be reimagined through an alternate prism for manmade structures.

4. Conclusions

Magnetic freeze casting was carried out with surface magnetized alumina particles (≈ 350 nm) and platelets (≈ 5 μm diameter, ≈ 200 nm thickness) at varying particle to platelet ratios (0:1, 1:3, 1:1, 3:1, 7:1, 1:0) and magnetic field strength (0, 75 mT). Aggregation of particles and platelets into chains at 75 mT that led to lamellar wall alignment in the *y*-axis was dependent on size, aspect ratio and a preponderance of either particles or platelets within the slurry system. Magnetometer data indicated larger magnetized platelets had greater interaction energy than smaller particles and ≈ 98% lamellar wall alignment in the *y*-axis was confirmed in homogeneous platelet scaffolds with scanning electron microscopy (SEM). Scaffold center regions from heterogeneous mixtures of particles and platelets (1:3, 1:1, 3:1, 7:1) were examined with SEM and lamellar wall alignment in the *y*-axis was observed in all, except for the 1:1 particle to platelet ratio condition. Microstructural ordering between dissimilar particles and platelets as well as long range lamellar wall alignment (≈ 60%) in the *y*-axis were most evident in 7:1 particle to platelet scaffolds. Young's modulus (≈ 225%) and strength (≈ 40%) were both enhanced in the *y*-axis for 7:1 particle to platelet scaffolds. Previous magnetic freeze casting work with different sized magnetized alumina particles and magnetic field strengths was further expounded upon using varying ratios of magnetized particles and platelets freeze cast at an optimal magnetic field strength (75 mT). Microstructural resemblance of 7:1 particle to platelet scaffolds to light-frame wood construction with shear wall sheathing and studs can extend inspiration sources beyond the bioinspired.

Acknowledgements

This work is supported by a Multi-University Research Initiative (MURI) through the Air Force Office of Scientific Research of the United States (AFOSR-FA9550-15-1-0009) and a National Science Foundation Biomaterials Program Grant 1507978. The authors wish to acknowledge students who assisted with magnetic freeze casting and mechanical testing at University of California, San Diego (Jerry Ng and Ali Ismail). We thank Prof. Marc A. Meyers (University of California, San Diego) for assistance with mechanical characterization and Ryan Anderson (University of California, San Diego) for SEM micrographs of magnetized particles. Last, but certainly not least, we sincerely appreciate all the efforts of the amazing Ms. Ayaka Yamaguchi from Kinsei Matec Co., Ltd. (Osaka, Japan), as well as the company itself, for supplying us with a variety of alumina platelet samples to work with throughout our experiments. These experiments would not have been possible without their continuous exemplary support.

Appendix A. Supporting information

Supplementary data associated with this article can be found in the online version at http://dx.doi.org/10.1016/j.jmbbm.2017.06.002.

References

Abba, M.T., Hunger, P.M., Kalidindi, S.R., Wegst, U.G.K., 2016. Nacre-like hybrid films: structure, properties, and the effect of relative humidity. J. Mech. Behav. Biomed. Mater. 55, 140–150.

Aizenberg, J., Fratzl, P., 2013. New materials through bioinspiration and nanoscience. Adv. Funct. Mater. 23 (36), 4398–4399.

Amorin, H., Kholkin, A.L., Costa, M.E.V., 2008. Templated grain growth of SrBi2Ta2O9 ceramics: mechanism of texture development. Mater. Res. Bull. 43 (6), 1412–1419.

Andreu, J.S., Camacho, J., Faraudo, J., 2011. Aggregation of superparamagnetic colloids in magnetic fields: the quest for the equilibrium state. Soft Matter 7 (6), 2336–2339.

Bai, H., Chen, Y., Delattre, B., Tomsia, A.P., Ritchie, R.O., 2015. Bioinspired large-scale aligned porous materials assembled with dual temperature gradients. Sci. Adv. 1 (11), e1500849.

Bai, H., Walsh, F., Gludovatz, B., Delattre, B., Huang, C.L., Chen, Y., Tomsia, A.P., Ritchie, R.O., 2016. Bioinspired hydroxyapatite/Poly(methyl methacrylate) composite with a nacre-mimetic architecture by a bidirectional freezing method. Adv. Mater. 28 (1), 50–56.

Bouville, F., Maire, E., Meille, S., Van de Moortele, B., Stevenson, A.J., Deville, S., 2014. Strong, tough and stiff bioinspired ceramics from brittle constituents. Nat. Mater. 13 (5), 508–514.

Bouville, F., Portuguez, E., Chang, Y.F., Messing, G.L., Stevenson, A.J., Maire, E., Courtois, L., Deville, S., 2014. Templated grain growth in macroporous materials. J. Am. Ceram. Soc. 97 (6), 1736–1742.

Bouville, F., Maire, E., Deville, S., 2014. Self-assembly of faceted particles triggered by a moving ice front. Langmuir 30 (29), 8656–8663.

Bowen, P., Sheng, J., Jongen, N., 2002. Particle size distribution measurement of anisotropic-particles cylinders and platelets - practical examples. Powder Technol. 128 (2–3), 256–261.

Cahill, J.T., Ruppert, J.N., Wallis, B., Liu, Y.M., Graeve, O.A., 2014. Development of mesoporosity in Scandia-Stabilized Zirconia: particle size, solvent, and calcination effects. Langmuir 30 (19), 5585–5591.

Carisey, T., Laugierwerth, A., Brandon, D.G., 1995. Control of texture in Al2O3 by gel casting. J. Eur. Ceram. Soc. 15 (1), 1–8.

Carisey, T., Levin, I., Brandon, D.G., 1995. Microstructure and mechanical properties of textured Al2O3. J. Eur. Ceram. Soc. 15 (4), 283–289.

Chang, Y.F., Poterala, S., Yener, D., Messing, G.L., 2013. Fabrication of highly textured fine-grained alpha-alumina by templated grain growth of nanoscale precursors. J. Am. Ceram. Soc. 96 (5), 1390–1397.

Chen, D.X., Sanchez, A., Taboada, E., Roig, A., Sun, N., Gu, H.C., 2009. Size determination of superparamagnetic nanoparticles from magnetization curve. J. Appl. Phys. 105 (8), 6.

Chen, S.L., Fan, C.M., Pan, J.L., 2010. Experimental study on full-scale light frame wood house under lateral load. J. Struct. Eng. -ASCE 136 (7), 805–812.

Deville, S., Saiz, E., Nalla, R.K., Tomsia, A.P., 2006. Freezing as a path to build complex composites. Science 311 (5760), 515–518.

Eckel, Z.C., Zhou, C.Y., Martin, J.H., Jacobsen, A.J., Carter, W.B., Schaedler, T.A., 2016. 3D printingadditive manufacturing of polymer-derived ceramics. Science 351 (6268), 58–62.

Erb, R.M., Libanori, R., Rothfuchs, N., Studart, A.R., 2012. Composites reinforced in three dimensions by using low magnetic fields. Science 335 (6065), 199–204.

Faraudo, J., Andreu, J.S., Camacho, J., 2013. Understanding diluted dispersions of superparamagnetic particles under strong magnetic fields: a review of concepts, theory and simulations. Soft Matter 9 (29), 6654–6664.

Faraudo, J., Andreu, J.S., Calero, C., Camacho, J., 2016. Predicting the self-assembly of superparamagnetic colloids under magnetic fields. Adv. Funct. Mater. 26 (22), 3837–3858.

Fathi, H., Kelly, J.P., Vasquez, V.R., Graeve, O.A., 2012. Ionic concentration effects on reverse micelle size and stability: implications for the synthesis of nanoparticles. Langmuir 28 (25), 9267–9274.

Frank, M.B., Naleway, S.E., Haroush, T., Liu, C.-H., Siu, S.H., Ng, J., Torres, I., Ismail, A., Karandikar, K., Porter, M.M., Graeve, O.A., McKittrick, J., 2017. Stiff porous scaffolds from magnetized alumina particles aligned by magnetic freeze casting. Mater. Sci. Eng.: C. 77, 484–492.

Ghosh, D., Dhavale, N., Banda, M., Kang, H., 2016. A comparison of microstructure and uniaxial compressive response of ice-templated alumina scaffolds fabricated from two different particle sizes. Ceram. Int. 42 (14), 16138–16147.

Ghosh, D., Banda, M., Kang, H., Dhavale, N., 2016. Platelets-induced stiffening and strengthening of ice-templated highly porous alumina scaffolds. Scr. Mater. 125, 29–33.

Ghosh, D., Kang, H., Banda, M., Kamaha, V., 2017. Influence of anisotropic grains (platelets) on the microstructure and uniaxial compressive response of ice-templated sintered alumina scaffolds. Acta Mater. 125, 1–14.

Graeve, O.A., Madadi, A., Kanakala, R., Sinha, K., 2010. Analysis of particle and crystallite size in tungsten nanopowdersynthesis,. Metall. Mater. Trans. A-Phys. Metall. Mater. Sci. 41A (10), 2691–2697.

Graeve, O.A., Fathi, H., Kelly, J.P., Saterlie, M.S., Sinha, K., Rojas-George, G., Kanakala, R., Brown, D.R., Lopez, E.A., 2013. Reverse micelle synthesis of oxide nanopowders: mechanisms of precipitate formation and agglomeration effects. J. Colloid Interface Sci. 407, 302–309.

Hall, P.W., Swinnea, J.S., Kovar, D., 2001. Fracture resistance of highly textured alumina. J. Am. Ceram. Soc. 84 (7), 1514–1520.

Hayakawa, O., Nakahira, K., Naito, M., Tsubaki, J., 1998. Experimental analysis of sample preparation conditions for particle size measurement. Powder Technol. 100 (1), 61–68.

Huiskes, R., 2000. If bone is the answer, then what is the question? J. Anat. 197, 145–156.

Hunger, P.M., Donius, A.E., Wegst, U.G.K., 2013. Structure-property-processing correlations in freeze-cast composite scaffolds. Acta Biomater. 9 (5), 6338–6348.

Hunger, P.M., Donius, A.E., Wegst, U.G., 2013. Platelets self-assemble into porous nacre during freeze casting. J. Mech. Behav. Biomed. Mater. 19, 87–93.

Inoue, K., Sassa, K., Yokogawa, Y., Sakka, Y., Okido, M., Asai, S., 2003. Control of crystal orientation of hydroxyapatite by imposition of a high magnetic field. Mater. Trans. 44 (6), 1133–1137.

Kamperman, M., Burns, A., Weissgraeber, R., van Vegten, N., Warren, S.C., Gruner, S.M., Baiker, A., Wiesner, U., 2009. Integrating structure control over multiple length scales in porous high temperature ceramics with functional platinum nanoparticles. Nano Lett. 9 (7), 2756–2762.

Kan, Y.M., Wang, P.L., Li, Y.X., Cheng, Y.B., Yan, D.S., 2003. Fabrication of textured bismuth titanate by templated grain growth using aqueous tape casting. J. Eur. Ceram. Soc. 23 (12), 2163–2169.

Lee, S.H., Feng, L., Yin, J., Lee, J.S., Zhu, X., Suzuki, T.S., Sakka, Y., Tanaka, H., 2015. Dense SiC containing strongly aligned plate-like grains by magnetic treatment. Ceram. Int. 41 (3), 5079–5084.

Li, Y., Ellingwood, B.R., 2007. Reliability of woodframe residential construction subjected to earthquakes. Struct. Saf. 29 (4), 294–307.

Li, Y., Yin, Y.J., Ellingwood, B.R., Bulleit, W.M., 2010. Uniform hazard versus uniform risk bases for performance-based earthquake engineering of light-frame wood construction. Earthq. Eng. Struct. Dyn. 39 (11), 1199–1217.

van de Lindt, J.W., 2005. Damage-based seismic reliability concept for woodframe structures. J. Struct. Eng. -ASCE 131 (4), 668–675.

Miller, S.M., Xiao, X., Faber, K.T., 2015. Freeze-cast alumina pore networks: effects of freezing conditions and dispersion medium. J. Eur. Ceram. Soc. 35 (13), 3595–3605.

Munch, E., Launey, M.E., Alsem, D.H., Saiz, E., Tomsia, A.P., Ritchie, R.O., 2008. Tough, Bio-Inspired Hybrid. Mater., Sci. 322 (5907), 1516–1520.

Munch, E., Saiz, E., Tomsia, A.P., Deville, S., 2009. Architectural control of freeze-cast ceramics through additives and templating. J. Am. Ceram. Soc. 92 (7), 1534–1539.

Naglieri, V., Bale, H.A., Gludovatz, B., Tomsia, A.P., Ritchie, R.O., 2013. On the development of ice-templated silicon carbide scaffolds for nature-inspired structural materials. Acta Mater. 61 (18), 6948–6957.

Naleway, S.E., Yu, C.F., Porter, M.M., Sengupta, A., Iovine, P.M., Meyers, M.A., McKittrick, J., 2015. Bioinspired composites from freeze casting with clathrate hydrates. Mater. Des. 71, 62–67.

Naleway, S.E., Fickas, K.C., Maker, Y.N., Meyers, M.A., McKittrick, J., 2016. Reproducibility of ZrO2-based freeze casting for biomaterials. Mater. Sci. Eng. C-Mater. Biol. Appl. 61, 105–112.

Niebel, T.P., Carnelli, D., Binelli, M.R., Libanori, R., Studart, A.R., 2016. Hierarchically roughened microplatelets enhance the strength and ductility of nacre-inspired composites. J. Mech. Behav. Biomed. Mater. 60, 367–377.

Nocera, T.M., Chen, J., Murray, C.B., Agarwal, G., 2012. Magnetic anisotropy considerations in magnetic force microscopy studies of single superparamagnetic nanoparticles. Nanotechnology 23 (49), 495704.

Oyanedel-Craver, V.A., Smith, J.A., 2008. Sustainable colloidal-silver-impregnated ceramic filter for point-of-use water treatment. Environ. Sci. Technol. 42 (3), 927–933.

Ozen, M., Mertens, M., Snijkers, F., Van Tendeloo, G., Cool, P., 2016. Texturing of hydrothermally synthesized BaTiO3 in a strong magnetic field by slip casting. Ceram. Int. 42 (4), 5382–5390.

Ozer, I.O., Suvaci, E., Karademir, B., Missiaen, J.M., Carry, C.P., Bouvard, D., 2006. Anisotropic sintering shrinkage in alumina ceramics containing oriented platelets. J. Am. Ceram. Soc. 89 (6), 1972–1976.

Paek, Y.K., Suvaci, E., Messing, G.L., 2002. Preparation and fracture behavior of alumina platelet reinforced alumina-monazite composites. Mater. Trans. 43 (12), 3262–3265.

Plappally, A.K., Yakub, I., Brown, L.C., Soboyejo, W.O., Soboyejo, A.B.O., 2011. Physical properties of porous clay ceramic-ware. J. Eng. Mater. Technol. -Trans. ASME 133 (3), 9.

Popat, K.C., Mor, G., Grimes, C., Desai, T.A., 2004. Poly (ethylene glycol) grafted nanoporous alumina membranes. J. Membr. Sci. 243 (1–2), 97–106.

Porter, M.M., Yeh, M., Strawson, J., Goehring, T., Lujan, S., Siripasopsotorn, P., Meyers, M.A., McKittrick, J., 2012. Magnetic freeze casting inspired by nature. Mater. Sci.

Eng. A-Struct. Mater. Prop. Microstruct. Process. 556, 741–750.
Porter, M.M., Imperio, R., Wen, M., Meyers, M.A., McKittrick, J., 2014. Bioinspired scaffolds with varying pore architectures and mechanical properties. Adv. Funct. Mater. 24 (14), 1978–1987.
Porter, M.M., Meraz, L., Calderon, A., Choi, H.J., Chouhan, A., Wang, L., Meyers, M.A., McKittrick, J., 2015. Torsional properties of helix-reinforced composites fabricated by magnetic freeze casting. Compos. Struct. 119, 174–184.
Porter, M.M., Niksiar, P., McKittrick, J., 2016. Microstructural control of colloidal-based ceramics by directional solidification under weak magnetic fields. J. Am. Ceram. Soc.
du Preez, M., Conroy, R.M., Wright, J.A., Moyo, S., Potgieter, N., Gundry, S.W., 2008. Short report: use of ceramic water filtration in the prevention of diarrheal disease: a randomized controlled trial in rural South Africa and Zimbabwe. Am. J. Trop. Med. Hyg. 79 (5), 696–701.
Sakka, Y., Suzuki, T.S., 2005. Textured development of feeble magnetic ceramics by colloidal processing under high magnetic field. J. Ceram. Soc. Jpn. 113 (1313), 26–36.
Saterlie, M., Sahin, H., Kavlicoglu, B., Liu, Y.M., Graeve, O., 2011. Particle size effects in the thermal conductivity enhancement of copper-based nanofluids. Nanoscale Res. Lett. 6, 7.
Saterlie, M.S., Sahin, H., Kavlicoglu, B., Liu, Y.M., Graeve, O.A., 2012. Surfactant effects on dispersion characteristics of copper-based nanofluids: a dynamic light scattering study. Chem. Mater. 24 (17), 3299–3306.
Seabaugh, M.M., Kerscht, I.H., Messing, G.L., 1997. Texture development by templated grain growth in liquid-phase-sintered alpha-alumina. J. Am. Ceram. Soc. 80 (5), 1181–1188.
A.W. Smith, (inventor), Boeing, (assignee), Process for producing an anodic aluminum oxide membrane, U.S. patent 3, 850, 762, 1974, Nov 26).
Snel, M.D., van Hoolst, J., de Wilde, A.M., Mertens, M., Snijkers, F., Luyten, J., 2009. Influence of tape cast parameters on texture formation in alumina by templated grain growth. J. Eur. Ceram. Soc. 29 (13), 2757–2763.
Studart, A.R., Gonzenbach, U.T., Tervoort, E., Gauckler, L.J., 2006. Processing routes to macroporous ceramics: a review. J. Am. Ceram. Soc. 89 (6), 1771–1789.
Suvaci, E., Seabaugh, M.M., Messing, G.L., 1999. Reaction-based processing of textured alumina by templated grain growth. J. Eur. Ceram. Soc. 19 (13–14), 2465–2474.
Suzuki, T.S., Sakka, Y., 2002. Fabrication of textured titania by slip casting in a high magnetic field followed by heating. Jpn. J. Appl. Phys. Part 2 – Lett. 41 (11A), L1272–L1274.
Suzuki, T.S., Sakka, Y., 2002. Control of texture in ZnO by slip casting in a strong magnetic field and heating. Chem. Lett. 12, 1204–1205.
Suzuki, T.S., Uchikoshi, T., Sakka, Y., 2006. Control of texture in alumina by colloidal processing in a strong magnetic field. Sci. Technol. Adv. Mater. 7 (4), 356–364.
Suzuki, T.S., Miwa, Y., Kawada, S., Kimura, M., Uchikoshi, T., Sakka, Y., 2013. Two-dimensional orientation in Bi4Ti3O12 prepared using platelet particles and a magnetic field. J. Am. Ceram. Soc. 96 (4), 1085–1089.
Takatori, K., Kadoura, H., Matsuo, H., Arakawa, S., Tani, T., 2016. Microstructural evolution of high purity alumina ceramics prepared by a templated grain growth method. J. Ceram. Soc. Jpn. 124 (4), 432–441.
Takenaka, T., Sakata, K., 1980. Grain orientation and electrical properties of hot forged Bi4Ti3O12 ceramics. Jpn. J. Appl. Phys. 19 (1), 31–39.
Tallon, C., Moreno, R., Nieto, M.I., 2009. Shaping of porous alumina bodies by freeze casting. Adv. Appl. Ceram. 108 (5), 307–313.
Tan, Y.M., Cervantes, O., Nam, S., Molitoris, J.D., Hooper, J.P., 2016. Dynamic fragmentation of cellular, ice-templated alumina scaffolds. J. Appl. Phys. 119 (2), 8.
Vargas-Consuelos, C.I., Seo, K., Camacho-Lopez, M., Graeve, O.A., 2014. Correlation between particle size and Raman vibrations in WO3 powders. J. Phys. Chem. C 118 (18), 9531–9537.
Vriami, D., Damjanovic, D., Vleugels, J., Van der Biest, O., 2015. Textured BaTiO3 by templated grain growth and electrophoretic deposition. J. Mater. Sci. 50 (24), 7896–7907.
Vriami, D., Beaugnon, E., Erauw, J.P., Vleugels, J., Van der Biest, O., 2015. Texturing of 3Y-TZP zirconia by slip casting in a high magnetic field of 17.4 T. J. Eur. Ceram. Soc. 35 (14), 3959–3967.
Wang, H., Chen, Q.W., Sun, L.X., Qi, H.P., Yang, X., Zhou, S., Xiong, J., 2009. Magnetic-field-induced formation of one-dimensional magnetite nanochains. Langmuir 25 (12), 7135–7139.
Wegst, U.G.K., Bai, H., Saiz, E., Tomsia, A.P., Ritchie, R.O., 2015. Bioinspired structural materials. Nat. Mater. 14 (1), 23–36.
Wei, M., Zhi, D., Brandon, D.G., 2005. Microstructure and texture evolution in gel-cast alpha-alumina/alumina platelet ceramic composites. Scr. Mater. 53 (12), 1327–1332.
Weiner, S., Wagner, H.D., 1998. The material bone: structure mechanical function relations. Annu. Rev. Mater. Sci. 28, 271–298.
Willie, B., Duda, G.N., Weinkamer, R., 2013. Bone structural adaptation and Wolff's law. In: Fratzl, P., Dunlop, J.W.C., Weinkamer, R. (Eds.), Materials Design Inspired by Nature: Function through Inner Architecture. Royal Soc Chemistry, Cambridge, pp. 17–45.
Wu, W.W., Sakka, Y., Suzuki, T.S., Zhang, G.J., 2014. Microstructure and anisotropic properties of textured ZrB2 and ZrB2-MoSi2 ceramics prepared by strong magnetic field alignment. Int. J. Appl. Ceram. Technol. 11 (2), 218–227.
Yang, Z.G., Yu, J.B., Li, C.J., Zhong, Y.B., Xuan, W.D., Ren, Z.M., Wang, Q.L., Dai, Y.M., Wang, H., 2015. Preparation of textured porous Al2O3 ceramics by slip casting in a strong magnetic field and its mechanical properties. Cryst. Res. Technol. 50 (8), 645–653.
Yoshizawa, Y., Toriyama, M., Kanzaki, S., 2001. Fabrication of textured alumina by high-temperature deformation. J. Am. Ceram. Soc. 84 (6), 1392–1394.
Zhang, H.F., Hussain, I., Brust, M., Butler, M.F., Rannard, S.P., Cooper, A.I., 2005. Aligned two- and three-dimensional structures by directional freezing of polymers and nanoparticles. Nat. Mater. 4 (10), 787–793.
Zhang, L., Vleugels, J., Van der Biest, O., 2010. Fabrication of textured alumina by orienting template particles during electrophoretic deposition. J. Eur. Ceram. Soc. 30 (5), 1195–1202.